using a film-less computed radiography (CR) system and gadolinium-based contrast media. In angiography of non-living animals, we observed fine blood vessels of approximately 100 μm with high contrasts.
© 2006 Elsevier Ltd. All rights reserved.

PACS: 52.59.Mv; 52.80.Vp; 87.59.Dj; 87.64.Gb

Keywords: Angiography; Gadolinium-based contrast media; Characteristic X-rays; Quasi-monochromatic X-rays; Tungsten K_α lines

1. Introduction

The successful uses of monochromatic parallel beams from synchrotron orbital radiation in recent years have greatly increased the demand for phase-contrast radiography (Davis et al., 1995; Momose et al., 1996; Ando et al., 2002) and enhanced K-edge angiography (Thompson et al., 1992; Mori et al., 1996; Hyodo et al., 1998). In particular, the parallel beams with photon energies of approximately 35 keV have been employed to perform angiography, because the beams are absorbed effectively by iodine-based contrast media with a K-absorption edge of 33.2 keV. Without using a synchrotron, we have developed an X-ray generator utilizing a cerium-target tube, and have performed cone-beam K-edge angiography achieved with cerium K_α rays of 34.6 keV (Sato et al., 2004a, b, c).

Gadolinium-based contrast media with a K-edge of 50.2 keV have been employed to perform magnetic resonance angiography (MRA), and the gadolinium density has been increasing. In view of this situation, ytterbium K_α rays (52.0 keV) are useful for enhanced K-edge angiography, because the K_α rays are absorbed effectively by gadolinium media. As compared with angiography using iodine media, the absorbed dose can be decreased considerably utilizing angiography achieved with gadolinium media. However, because ytterbium is a lanthanide series element and tends to oxidize in the atmosphere, K_α rays of tantalum (57.1 keV) and tungsten (58.9 keV) are also useful to perform angiography.

To produce high-dose-rate X-rays, several different flash X-ray generators have been developed (Sato et al., 1990, 1994a, b; Shikoda et al., 1994; Takahashi et al., 1994), and plasma flash X-ray generators (Sato et al., 2003a, b, 2004a, b, c, 2005a, b, c) have been developed to perform a preliminary experiment for producing hard X-ray lasers. In the plasma, the bremsstrahlung X-rays are absorbed effectively and are converted into fluorescent rays, and intense and clean K-series characteristic X-rays of nickel and copper have been produced from the axial direction of weakly ionized linear plasma. However, it is difficult to increase the photon energies of characteristic X-rays because the plasma transmits high-photon-energy bremsstrahlung X-rays. In view of this situation, we have developed a compact flash X-ray generator (Sato et al., 2004a, b, c, 2005a, b, c) and have succeeded in producing clean high-photon-energy characteristic X-rays utilizing the angle dependence of bremsstrahlung X-rays, because bremsstrahlung rays are not emitted in the opposite direction to that of electron trajectory in Sommerfeld's theory.

In this article, we describe an intense quasi-monochromatic plasma flash X-ray generator with a tungsten target tube, and used it to perform a preliminary study on angiography achieved with tungsten K_α rays.

2. Principle of K-edge angiography

Fig. 1 shows the mass attenuation coefficients of gadolinium at the selected energies; the coefficient curve is discontinuous at the gadolinium K-edge. The average photon energy of the tungsten K_α lines is shown above the gadolinium K-edge. The average photon energy is 58.9 keV, and gadolinium contrast media with a K-absorption edge of 50.2 keV absorb the lines easily. Therefore, blood vessels were observed with high contrasts.

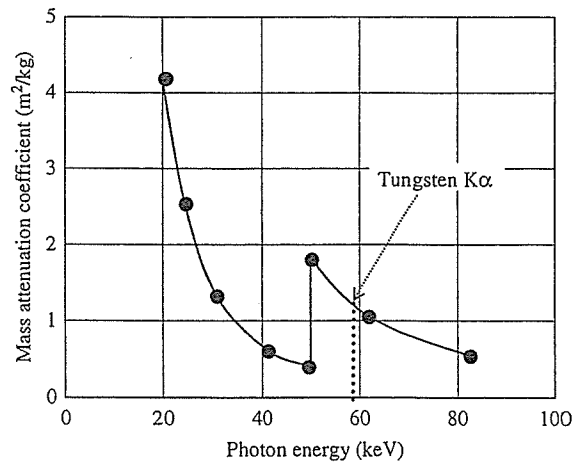

Fig. 1. Mass attenuation coefficients of gadolinium. The average photon energy of tungsten K_α lines is shown above gadolinium K edge.

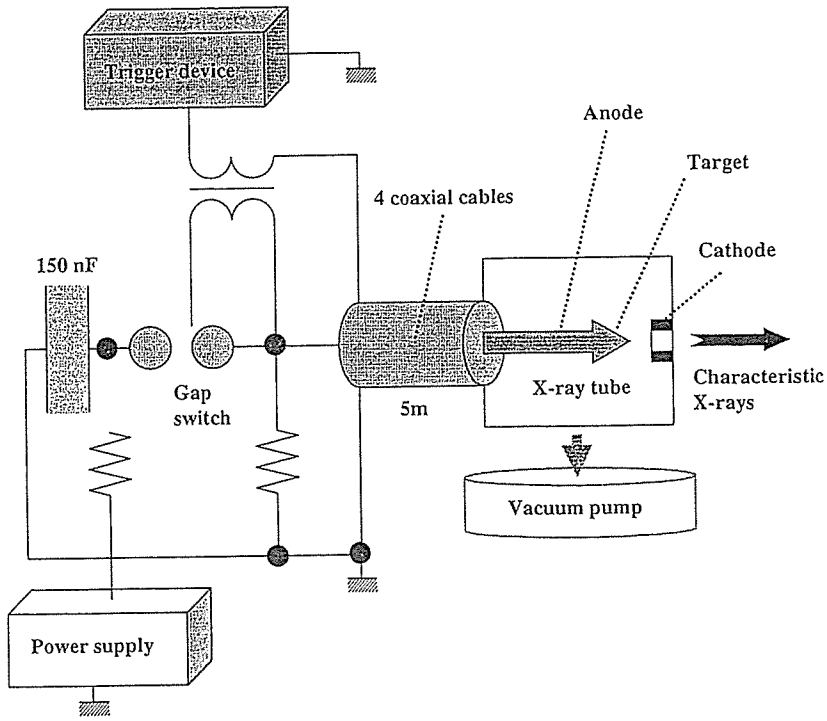

Fig. 2. Block diagram including the high-voltage circuit of the intense quasi-monochromatic plasma flash X-ray generator with a tungsten-target tube.

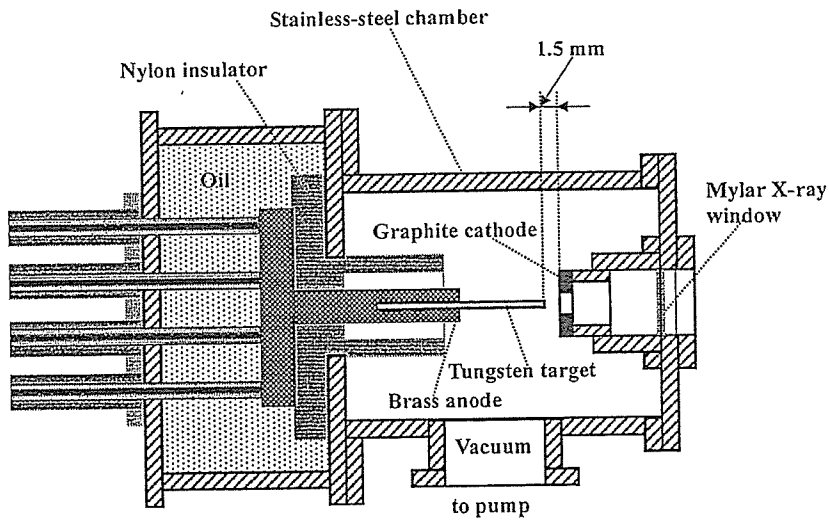

Fig. 3. Schematic drawing of a flash X-ray tube with a rod-shaped tungsten target.

3. Generator

3.1. High-voltage circuit

Fig. 2 shows a block diagram of a high-intensity plasma flash X-ray generator. The generator consists of the following essential components: a high-voltage power supply, a high-voltage condenser with a capacity of approximately 150 nF, an air gap switch, a turbomolecular pump, a thyratron pulse generator as a trigger device and a flash X-ray tube. In this generator, a coaxial cable transmission line is employed in order to

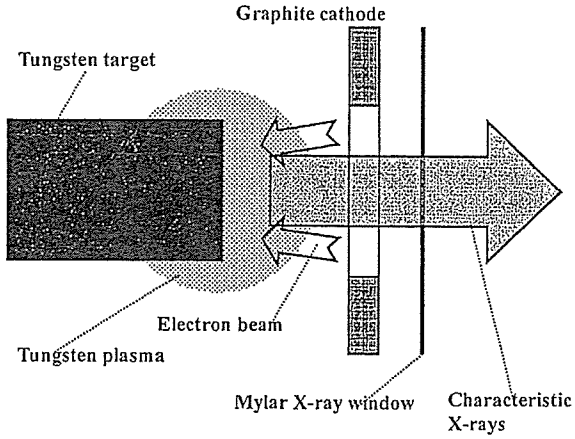

Fig. 4. Irradiation of K-series characteristic X-rays of tungsten.

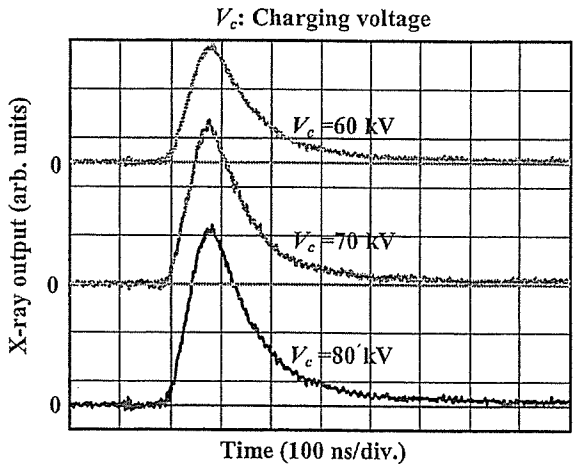

Fig. 5. X-ray outputs detected using a combination of a plastic scintillator and a photomultiplier.

increase maximum tube voltage using high-voltage reflection. The high-voltage main condenser is charged up to 80 kV by the power supply, and electric charges in the condenser are discharged to the tube through the four cables after closing the gap switch with the trigger device.

3.2. X-ray tube

The X-ray tube is a demountable cold-cathode diode that is connected to the turbomolecular pump with a pressure of approximately 1 mPa (Fig. 3). This tube consists of the following major parts: a ring-shaped graphite cathode with an inside diameter of 4.5 mm, a stainless-steel vacuum chamber, a nylon insulator, a polyethylene terephthalate (Mylar) X-ray window 0.25 mm in thickness and a rod-shaped tungsten target 3.0 mm in diameter. The distance between the target and cathode electrodes can be regulated from the outside of the tube, and is set to 1.5 mm. As electron beams from the cathode electrode are roughly converged to the target by the electric field in the tube, evaporation leads to the formation of weakly ionized plasma, consisting of tungsten ions and electrons, around the target. Because bremsstrahlung rays are not emitted in the opposite direction to that of electron trajectory (Fig. 4), tungsten K-series characteristic X-rays can be produced without using a filter.

4. Characteristics

4.1. Tube voltage and current

In this generator, it was difficult to measure the tube voltage and current since the tube voltages were high, and there was no space to set a current transformer for measuring the tube current. Currently, the voltage and

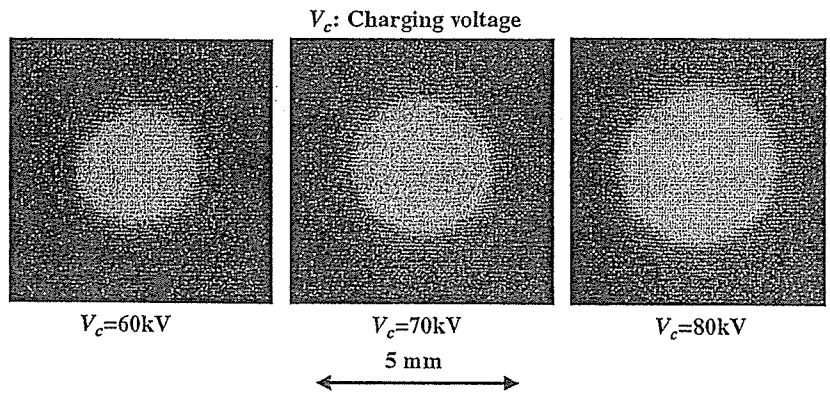

Fig. 6. Images of characteristic X-ray source obtained using a pinhole camera with changes in the charging voltage.

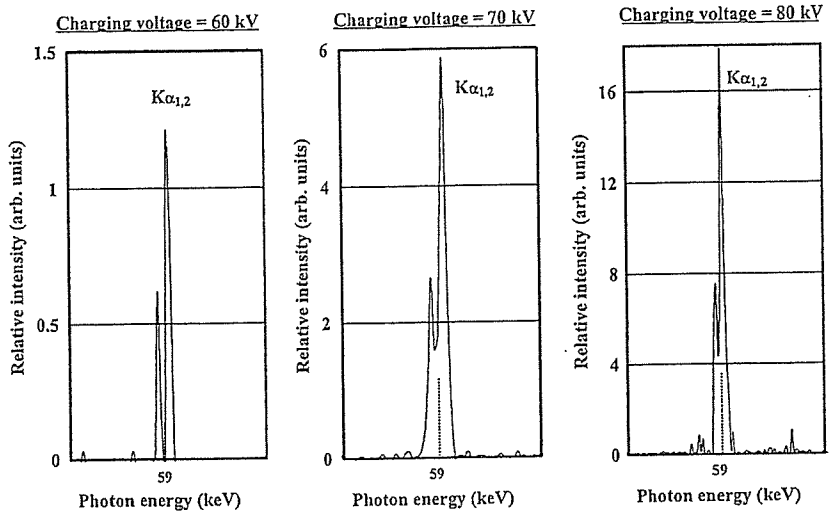

Fig. 7. X-ray spectra from a tungsten target. The spectra were measured using a transmission type spectrometer with a lithium fluoride curved crystal.

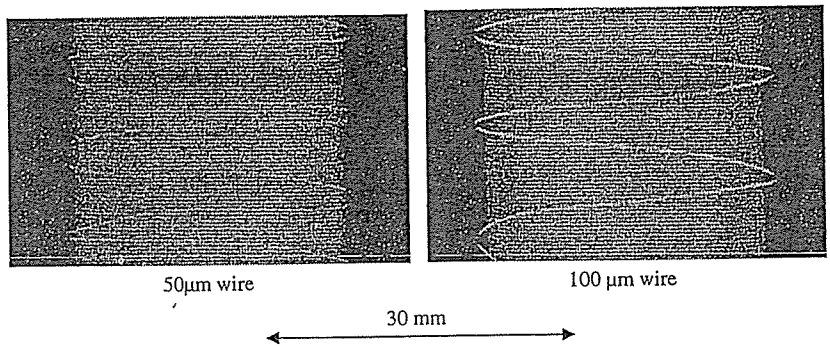

Fig. 8. Radiograms of tungsten wires coiled around rods made of polymethyl methacrylate.

current roughly display damped oscillations. When the charging voltage was increased, both the maximum tube voltage and current increased. At a charging voltage of 80 kV, the estimated maximum values of the tube voltage and current were approximately 160 kV (two times the charging voltage) and 40 kA, respectively.

4.2. X-ray output

X-ray output pulse was detected using a combination of a plastic scintillator and a photomultiplier (Fig. 5). The X-ray pulse height substantially increased with corresponding increases in the charging voltage. The X-ray pulse widths were approximately 110 ns, and the time-integrated X-ray intensity measured by a thermoluminescence dosimeter (Kyokko TLD Reader 1500 having MSO-S elements without energy compensation) had a value of approximately 0.35 mGy at 1.0 m from the X-ray source with a charging voltage of 80 kV.

4.3. X-ray source

In order to observe the plasma X-ray source, we employed a 100-μm-diameter pinhole camera and an X-ray film (Polaroid XR-7) (Fig. 6). When the charging voltage was increased, the plasma X-ray source grew, and both spot dimension and intensity increased. Because the X-ray intensity is the highest at the center of the spot, both the dimension and intensity decreased according to both increases in the thickness of a filter for absorbing X-rays and decreases in the pinhole diameter.

4.4. X-ray spectra

X-ray spectra were measured using a transmission-type spectrometer with a lithium fluoride curved crystal 0.5 mm in thickness. The X-ray intensities of the spectra were detected by an imaging plate of a computed radiography (CR) system (Sato et al., 2000) (Konica Minolta Regius 150) with a wide dynamic range, and

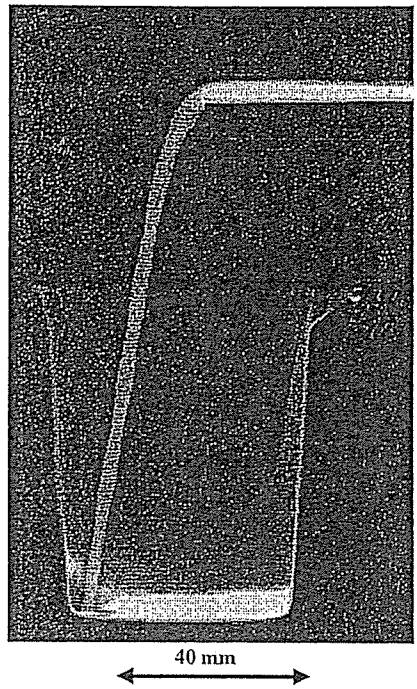

Fig. 9. Radiogram of water falling into polypropylene beaker from a glass test tube.

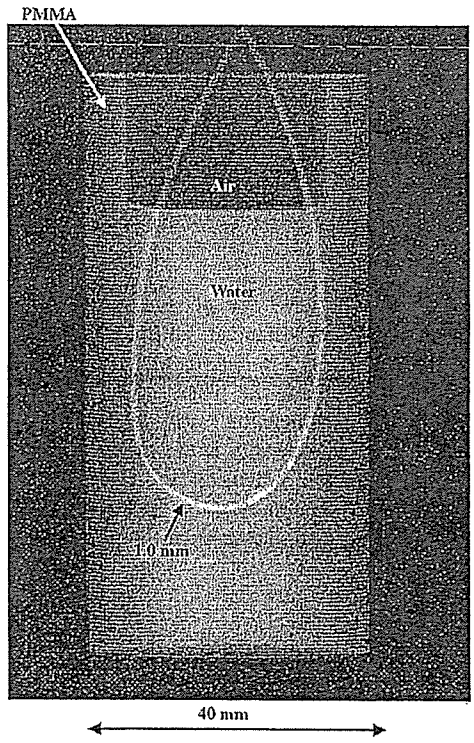

Fig. 10. Angiography of a Teflon tube using a contrast medium which contains approximately 65% gadodiamidehydrate.

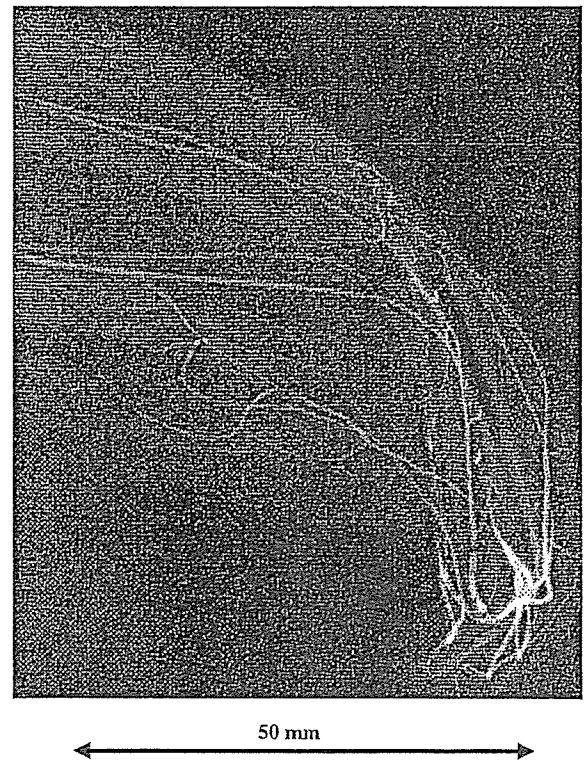

Fig. 11. Angiography of a rabbit ear using gadolinium oxide powder.

relative X-ray intensity was calculated from Dicom original digital data corresponding to X-ray intensity; the data was scanned by Dicom viewer in the film-less CR system. Subsequently, the relative X-ray intensity as a function of the data was calibrated using a conventional X-ray generator, and we confirmed that the intensity was proportional to the exposure time. Fig. 7 shows measured spectra from the tungsten target. We observed clean K_α lines, while bremsstrahlung rays were hardly detected. The K_α intensity substantially increased with increases in the charging voltage.

5. Angiography

The flash angiography was performed by the CR system at 1.2 m from the X-ray source, and the charging voltage was 80 kV.

Firstly, rough measurements of spatial resolution were made using wires. Fig. 8 shows radiograms of tungsten wires coiled around rods made of polymethyl methacrylate (PMMA). Although the image contrast decreased somewhat with decreases in the wire diameter, due to blurring of the image caused by the sampling pitch of 87.5 μm, a 50-μm-diameter wire could be observed.

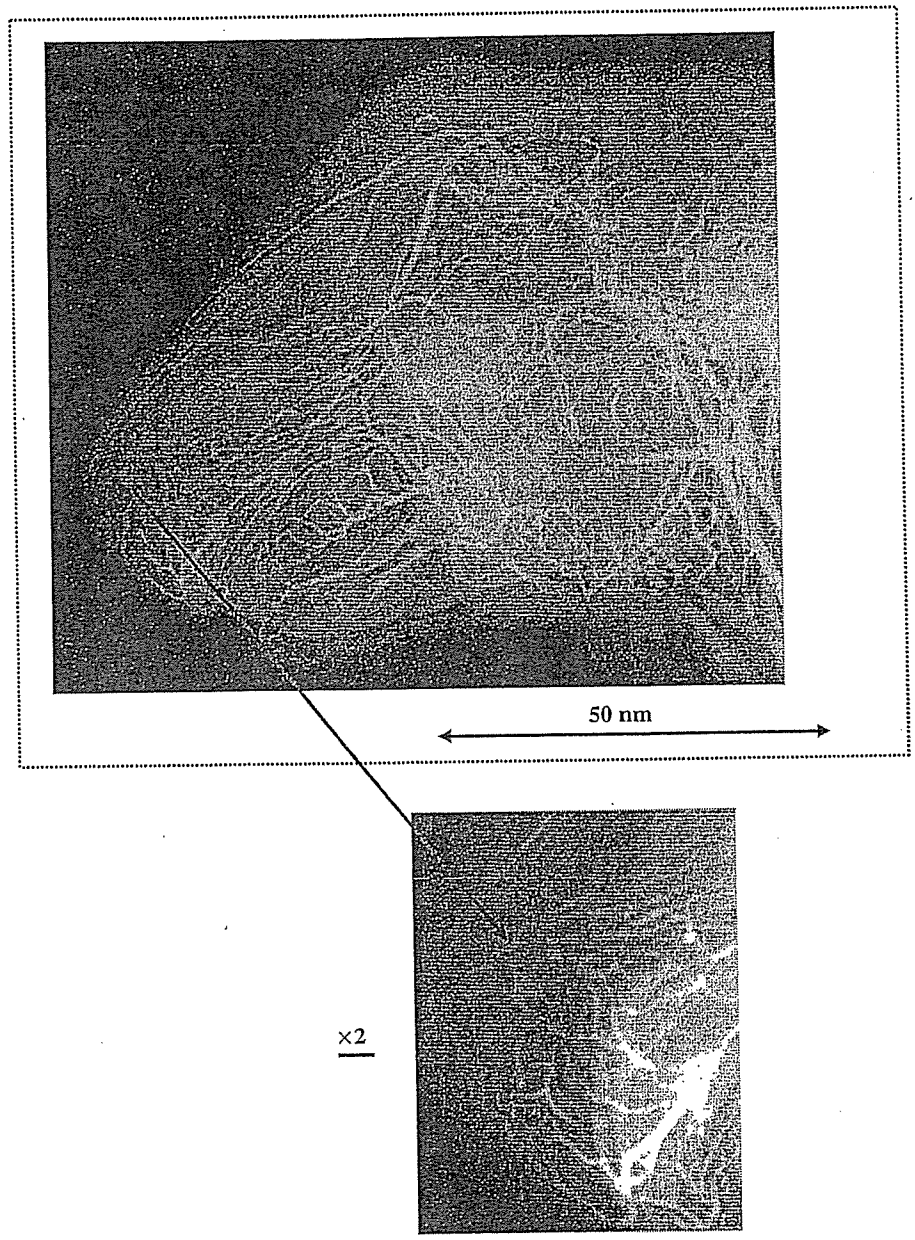

Fig. 12. Angiography of a rabbit head using gadolinium oxide powder.

The image of water (20% gadolinium oxide suspension) falling into a polypropylene beaker from a plastic test tube is shown in Fig. 9. The diameter of gadolinium oxide powder ranges from 1 to 10 μm. Because the X-ray duration was about 100 ns, the stop-motion image of water could be obtained.

Fig. 10 shows an angiogram of a polytetrafluoroethylene (Teflon) tube in a PMMA case using a contrast medium which contains approximately 65% gadodiamidehydrate, and a high-contrast tube with a bore diameter of 1.0 mm is observed. Figs. 11 and 12 show angiograms of a rabbit ear and head using gadolinium oxide powder, and fine blood vessels of approximately 100 μm were visible.

6. Conclusions and outlook

In summary, we succeeded in producing K_α rays of tungsten and in performing K-edge angiography using gadolinium contrast media with a K-edge of 50.2 keV, and this K-edge angiography could be a useful technique

to decrease the dose absorbed by patients. Although we employed tungsten K_α (58.9 keV) rays, L-series characteristic rays should be absorbed before angiography using a filter.

We obtained sufficient X-ray intensity for CR angiography with X-ray durations of approximately 100 ns, and the intensity can be increased by increasing the charging voltage at a constant target–cathode space. In an empirical equation, because the characteristic X-ray intensity is proportional to approximately 1.5th power of the voltage difference between the tube voltage and the critical excitation voltage, optimum intensity for angiography can be controlled. In this research, the generator produced instantaneous number of K photons was approximately 1×10^9 photons/cm^2 per pulse at 1.0 m from the source.

Because the dimensions of the X-ray source are primarily determined by the target diameter, the diameter should be minimized in order to improve the spatial resolution, and can be reduced to approximately 0.5 mm. Subsequently, the sampling pitch can be decreased to 43.8 μm using a CR system (Konica Minolta Regius 190) to observe fine blood vessels of approximately 50 μm diameter.

Using this flash X-ray generator, enhanced K-edge angiography using iodine contrast media can also be performed using a cerium target. In addition, steady-state monochromatic X-rays can be produced by a similar tube utilizing a hot cathode and a constant high-voltage power supply. In addition, fine focusing can be realized using tungsten or molybdenum target, and these X-ray generators could be employed to perform quasi-monochromatic phase-contrast radiography for edge enhancement.

Acknowledgments

This work was supported by Grants-in-Aid for Scientific Research (13470154, 13877114, 16591181 and 16591222) and Advanced Medical Scientific Research from MECSST, Health and Labor Sciences Research Grants (RAMT-nano-001, RHGTEFB-genome-005 and RHGTEFB-saisei-003), grants from the Keiryo Research Foundation, the Promotion and Mutual Aid Corporation for Private Schools of Japan, the Japan Science and Technology Agency (JST) and the New Energy and Industrial Technology Development Organization (NEDO, Industrial Technology Research Grant Program in 2003).

References

Ando, M., Maksimenko, M., Sugiyama, H., Pattanasiriwisawa, W., Hyodo, K., Uyama, C., 2002. A simple X-ray dark- and bright-field imaging using achromatic Laue optics. Jpn. J. Appl. Phys. 41, L1016–L1018.

Davis, T.J., Gao, D., Gureyev, T.E., Stevenson, A.W., Wilkins, S.W., 1995. Phase-contrast imaging of weakly absorbing materials using hard X-rays. Nature 373, 595–597.

Hyodo, K., Ando, M., Oku, Y., Yamamoto, S., Takeda, T., Itai, Y., Ohtsuka, S., Sugishita, Y., Tada, J., 1998. Development of a two-dimensional imaging system for clinical applications of intravenous coronary angiography using intense synchrotron radiation produced by a multipole wiggler. J. Synchrotron Rad. 5, 1123–1126.

Momose, A., Takeda, T., Itai, Y., Hirano, K., 1996. Phase-contrast X-ray computed tomography for observing biological soft tissues. Nat. Med. 2, 473–475.

Mori, H., Hyodo, K., Tanaka, E., Mohammed, M.U., Yamakawa, A., Shinozaki, Y., Nakazawa, H., Tanaka, Y., Sekka, T., Iwata, Y., Honda, S., Umetani, K., Ueki, H., Yokoyama, T., Tanioka, K., Kubota, M., Hosaka, H., Ishizawa, N., Ando, M., 1996. Small-vessel radiography in situ with monochromatic synchrotron radiation. Radiology 201, 173–177.

Sato, E., Kimura, S., Kawasaki, S., Isobe, H., Takahashi, K., Tamakawa, Y., Yanagisawa, T., 1990. Repetitive flash X-ray generator utilizing a simple diode with a new type of energy-selective function. Rev. Sci. Instrum. 61, 2343–2348.

Sato, E., Takahashi, K., Sagae, M., Kimura, S., Oizumi, T., Hayasi, Y., Tamakawa, Y., Yanagisawa, T., 1994a. Sub-kilohertz flash X-ray generator utilizing a glass-enclosed cold-cathode triode. Med. Biol. Eng. Comput. 32, 289–294.

Sato, E., Sagae, M., Takahashi, K., Shikoda, A., Oizumi, T., Hayasi, Y., Tamakawa, Y., Yanagisawa, T., 1994b. 10kHz microsecond pulsed X-ray generator utilizing a hot-cathode triode with variable durations for biomedical radiography. Med. Biol. Eng. Comput. 32, 295–301.

Sato, E., Sato, K., Tamakawa, Y., 2000. Film-less computed radiography system for high-speed imaging. Ann. Rep. Iwate Med. Univ. Sch. Lib. Arts Sci. 35, 13–23.

Sato, E., Hayasi, Y., Germer, R., Tanaka, E., Mori, H., Kawai, T., Obara, H., Ichimaru, T., Takayama, K., Ido, H., 2003a. Irradiation of intense characteristic X-rays from weakly ionized linear molybdenum plasma. Jpn. J. Med. Phys. 23, 123–131.

Sato, E., Hayasi, Y., Germer, R., Tanaka, E., Mori, H., Kawai, T., Ichimaru, T., Takayama, K., Ido, H., 2003b. Quasi-monochromatic flash X-ray generator utilizing weakly ionized linear copper plasma. Rev. Sci. Instrum. 74, 5236–5240.

Sato, E., Sagae, M., Tanaka, E., Hayasi, Y., Germer, R., Mori, H., Kawai, T., Ichimaru, T., Sato, S., Takayama, Y., Ido, H., 2004a. Quasi-monochromatic flash X-ray generator utilizing a disk-cathode molybdenum tube. Jpn. J. Appl. Phys. 43, 7324–7328.

Sato, E., Hayasi, Y., Germer, R., Tanaka, E., Mori, H., Kawai, T., Ichimaru, T., Sato, S., Takayama, K., Ido, H., 2004b. Sharp characteristic X-ray irradiation from weakly ionized linear plasma. J. Electron Spectrosc. Related Phenom. 137–140, 713–720.

Sato, E., Tanaka, E., Mori, H., Kawai, T., Ichimaru, T., Sato, S., Takayama, K., Ido, H., 2004c. Demonstration of

enhanced K-edge angiography using a cerium target X-ray generator. Med. Phys. 31, 3017–3021.

Sato, E., Tanaka, E., Mori, H., Kawai, T., Ichimaru, T., Sato, S., Takayama, Y., Ido, H., 2005a. Compact monochromatic flash X-ray generator utilizing a disk-cathode molybdenum tube. Med. Phys. 32, 49–54.

Sato, E., Tanaka, E., Mori, H., Kawai, T., Sato, S., Takayama, Y., 2005b. High-speed enhanced K-edge angiography utilizing cerium plasma X-ray generator. Opt. Eng. 44, 049001–049016.

Sato, E., Tanaka, E., Mori, H., Kawai, T., Sato, S., Takayama, Y., 2005c. Clean monochromatic X-ray irradiation from weakly ionized linear copper plasma. Opt. Eng. 44, 049002–049016.

Shikoda, A., Sato, E., Sagae, M., Oizumi, T., Tamakawa, Y., Yanagisawa, T., 1994. Repetitive flash X-ray generator having a high-durability diode driven by a two-cable-type line pulser. Rev. Sci. Instrum. 65, 850–856.

Takahashi, K., Sato, E., Sagae, M., Oizumi, T., Tamakawa, Y., Yanagisawa, T., 1994. Fundamental study on a long-duration flash X-ray generator with a surface-discharge triode. Jpn. J. Appl. Phys. 33, 4146–4151.

Thompson, A.C., Zeman, H.D., Brown, G.S., Morrison, J., Reiser, P., Padmanabahn, V., Ong, L., Green, S., Giacomini, J., Gordon, H., Rubenstein, E., 1992. First operation of the medical research facility at the NSLS for coronary angiography. Rev. Sci. Instrum. 63, 625–628.

ELSEVIER

Cardiovascular Research 72 (2006) 412–421

Cardiovascular Research

www.elsevier.com/locate/cardiores

Heavy ion radiation up-regulates Cx43 and ameliorates arrhythmogenic substrates in hearts after myocardial infarction

Mari Amino [a,f,1], Koichiro Yoshioka [a,1], Teruhisa Tanabe [a], Etsuro Tanaka [b], Hidezo Mori [c], Yoshiya Furusawa [d], Wojciech Zareba [e], Masatoshi Yamazaki [f], Harumichi Nakagawa [f], Haruo Honjo [f], Kenji Yasui [f], Kaichiro Kamiya [f], Itsuo Kodama [f,*]

[a] *Department of Cardiology, Tokai University School of Medicine, Isehara, Japan*
[b] *Department of Nutritional Sciences, Tokyo University of Agriculture, Tokyo, Japan*
[c] *Department of Cardiac Physiology, National Cardiovascular Center Research Institute, Osaka, Japan*
[d] *National Institute of Radiological Sciences, Chiba, Japan*
[e] *Cardiology Unit, University of Rochester, Rochester, USA*
[f] *Research Institute of Environmental Medicine, Nagoya University, Nagoya, Japan*

Received 4 June 2006; received in revised form 12 September 2006; accepted 15 September 2006
Available online 20 September 2006
Time for primary review 17 days

Abstract

Objective: Radiation has been shown to enhance intercellular communication in the skin and lungs through an increase of connexin43 (Cx43) expression. If analogous Cx43 up-regulation is induced in the diseased heart, it would provide a new perspective in radiation therapy for arrhythmias. The aim of the present study is to test this hypothesis.

Methods: Non-transmural myocardial infarction (MI) was created in 24 rabbits by microsphere injection into the coronary arteries. Twenty-four rabbits without MI were used as controls. Targeted external heavy ion beam irradiation (THIR; 15 Gy) was applied 2 weeks after MI with an accelerator (HIMAC, Chiba, Japan).

Results: The THIR was associated with an increase of Cx43 mRNA and protein levels in the left ventricle in control as well as in MI rabbits. THIR also increased lateralization of Cx43, which was no longer colocalized with cadherins. In MI hearts, immunoreactive Cx43 signals were reduced in the peri-infarct zone, and the reduction was reversed by THIR. *In-vivo* epicardial potential mapping on the free wall (64 unipolar electrodes to cover 7 × 7 mm) in MI hearts revealed reduced conduction velocity, whereas dispersion of the activation-recovery interval (ARI) was increased compared with controls, and these changes were reversed by THIR. The vulnerability for ventricular tachyarrhythmias (VT/VF), which was estimated by programmed stimulation, was increased in MI hearts, and this increased vulnerability to arrhythmias was reversed by THIR.

Conclusions: THIR increases Cx43 expression, improves the conductivity, decreases the spatial heterogeneity of repolarization, and reduces the vulnerability of rabbit hearts to ventricular arrhythmias after MI. THIR could have an antiarrhythmic potential through an improvement of electrical coupling.

© 2006 European Society of Cardiology. Published by Elsevier B.V. All rights reserved.

Keywords: Gap junctions; Connexin43; Heavy ion radiaton; Myocardial infarction; Ventricular arrhythmias; Arrhythmia (mechanisms); Epicardial mapping

1. Introduction

Modalities currently available for treatment and prevention of life-threatening ventricular tachyarrhythmias (VT/VF) are antiarrhythmic drugs, catheter ablation and implantable cardioverter/defibrillator (ICD). The usefulness of these therapeutic options is limited by either low efficiency, intolerable side

* Corresponding author. Tel.: +81 52 789 3871; fax: +81 52 789 3890.
E-mail address: ikodama@riem.nagoya-u.ac.jp (I. Kodama).
[1] The first two authors contributed equally to this work.

0008-6363/$ - see front matter © 2006 European Society of Cardiology. Published by Elsevier B.V. All rights reserved.
doi:10.1016/j.cardiores.2006.09.010

effects, or impairment of the quality of life (QOL) of the recipient. Fundamentally innovative antiarrhythmic strategies are, therefore, a matter of great concern to cardiologists.

In the heart, gap junctions (GJs) provide the pathways of intercellular current flow, enabling coordinated action potential propagation and contraction. GJ-channels are constructed from connexins (Cx), a multigene family of conserved proteins. In the mammalian heart, connexin43 (Cx43) is the most abundant and ubiquitous. Deranged expression and organization of Cx43 GJs in the ventricular muscles have been demonstrated in a variety of diseased hearts including ischemia, hypertrophy and inflammatory cardiomyopathy [1]. Such GJs remodeling is supposed to create arrhythmogenic substrates by modulating the propagation of excitation. X-ray irradiation has been shown to increase intercellular communication in the mouse skin [2] and rat alveolar epithelial cells in the lung [3] through an increase of expression of Cx43. If analogous up-regulation of Cx43 by radiation is induced efficiently in the diseased heart, it would provide a new perspective in the treatment of arrhythmias.

Radiotherapy using heavy-ions to treat deep-seated cancer was started at the National Institute of Radiological Sciences (NIRS) in Chiba, Japan in 1994 [4]. Charged-ion beams such as accelerated carbon-ions show a unique depth-dose distribution referred to as the Bragg peak in the target matter [5]. Those energetic ion beams decrease in kinetic energy thus reducing the velocity, finally stopping at a defined depth in the target object with high linear energy transfer (LET) [6], indicating a high relative biological effectiveness to X-rays (RBE). This gives advantages to heavy-ions over other radionucleid species in cancer therapy [5,6]. Based on this oncological experience, we hypothesized that such targeted heavy-ion beam irradiation (THIR) could also offer an advantage in causing up-regulation of Cx43 in the ischemic myocardium with minimal damage to the surrounding tissues.

2. Methods

Animal-handling followed the *Guide for the Care and Use of Laboratory Animals* (NIH Publication 85–23, revised 1996) with procedures approved by the Animal-Experimentation Ethics Committee of the Tokai University.

2.1. Animal model and heavy ion radiation

New Zealand white rabbits (n=48) weighing 3.5–4.0 kg were used. Non-transmural patchy myocardial infarction (MI) was created in 24 rabbits by microsphere injection (15 μm in diameter, 5×10^5/mL, 3 mL) into the coronary arteries by the transcatheter approach introduced from the carotid arteries [7]. The remaining 24 rabbits served as controls. Two weeks later, each 12 of MI and control rabbits received targeted THIR. Therefore, 4 animal groups were prepared: Control (C), C+THIR, MI, and MI+THIR.

We used carbon-ion beams provided by the Heavy Ion Medical Accelerator in Chiba (HIMAC) at NIRS, Japan [4]. The antero-lateral left ventricular (LV) free wall was focused for irradiation with carbon-ion beams (15 Gy) through the left anterior breast. The dose setting was confirmed appropriate in a pilot study. More details regarding the THIR procedures are described in the online data supplement.

2.2. Histology and immunohistochemistry

Ventricular tissue sections (12 μm thick slices) were fixed and embedded in paraffin. To recognize the MI and fibrosis region, the sections were stained by both hematoxylin/eosin (HE) and azan. The amounts of fibrosis were estimated from the binary images of azan-staining (Fig. 1). For immunostaining, the sections were incubated with an anti-Cx43 mouse monoclonal antibody (Chemicon), and then were treated with the secondary antibody (Alexa Flour 488 conjugated anti-mouse IgG). Some sections were also labeled with Alexa Flour 594 conjugated anti-cadherin, mouse monoclonal antibody (abcam). The immunolabelled sections were examined with a laser confocal microscope (LSM510, Version 2.02), and analyzed with the CLSM macro program (Carl Zeiss).

2.3. Real-time PCR and Western blotting

To quantify mRNA expression of Cx43 in the LV free wall, we performed a real-time PCR assay (Perkin-Elmer ABI Prism7700) [8]. GAPDH mRNA was used as an internal control. Sequence of PCR primers and sequence-specific probes are shown in the online data supplement.

The amount of Cx43 protein was evaluated by Western blotting [9]. The intensity of the Cx43 bands was quantified by densitometry and normalized to α-tubulin as the control.

2.4. In-vivo experiments

In-vivo electrophysiology experiments were conducted following open thorax surgery under anesthesia (α-chloralose, 80 mg/kg and urethane, 1000 mg/kg) [10]. An array of 8×8 monopolar electrodes (64Map) to cover 7×7 mm square (interpolar distance, 1 mm) was put on the LV wall between the left anterior descending branch (LAD) and left circumflex branch (LCx) of coronary arteries (Fig. 5A) [10]. The 64Map signals recorded simultaneously were acquired and processed by a computer. Activation time (AT) was defined as the interval from the beginning of QRS to the initial sharp negative deflection (min dV/dt). Recovery time (RT) was defined as the interval from the beginning of QRS to max dV/dt of T wave. The time difference between AT and RT in each electrogram was measured for the activation-recovery interval (ARI) as an index of action potential duration [11]. The dispersion of ARI (ARID) in the mapped area was estimated by the standard deviation of ARI at 64 electrodes [12]. The earliest AT within the electrode array was set down as 0 ms. Total activation time (TAT) was assessed as the delay between activation of the first and activation of the last electrode [12].

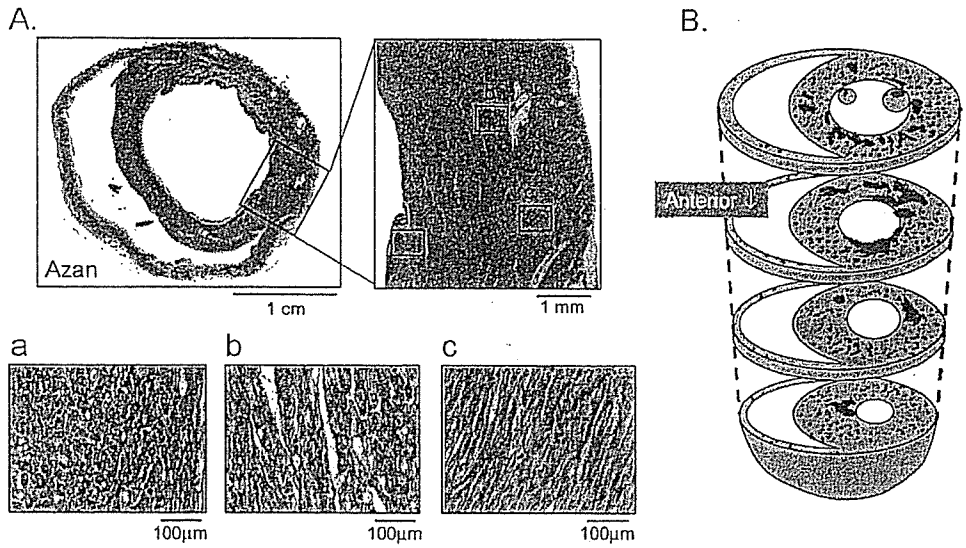

Fig. 1. Creation of non-transmural patchy myocardial infarction (MI) in rabbit hearts. A, a complete cross section of a low (left top), a moderate (right top) and a high magnification (bottom) of the ventricles 4 weeks after the creation of MI stained with HE/azan. Patchy fibrotic tissues (blue) are widely distributed in the subendocardial (a), mid-myocardial (b) and subepicardial (c) layers of the left ventricle (LV). B, 3-dimensional illustration of fibrotic tissue distribution (blue) in the same heart.

In order to assess the anisotropic conduction property, LV was paced at a cycle length of 200 ms (pulses of 1 ms duration and 1.2 times the threshold) via a pair of contiguous bipolar electrodes placed in the middle on the upper edge of the electrode array. Longitudinal (L) and transverse (T) directions of propagation were determined from the isochrone maps [9]. Conduction velocity (CV) was determined by linear regression of the isochrone distance vs. AT.

Propensity to VT/VF was tested by programmed electrical stimulation under norepinephrine infusion (0.1 μg/kg/min, i.v.). A pair of bipolar electrodes was placed on the epicardial surface near the LV apex. Following 5 basic stimuli (S1) at a cycle length of 200 ms, triple extra-stimuli (S2–S4) of double threshold were applied at progressively shorter coupling intervals.

2.5. Data analysis

Data are presented as means±SD. Data sets containing multiple groups were analyzed by 2-way layout analysis of variance and Bonferroni type multiple comparisons. Differences were considered statistically significant at a value of $P<0.05$.

3. Results

3.1. Standard light microscopy

Pathological features of rabbit hearts 4 weeks after creation of non-transmural MI by the microsphere injection method were analyzed in sections stained with HE and azan. Representative results (without radiation) are shown in Fig. 1. Multiple, small patchy infarctions with fibrosis surrounded by noninfarcted myocardium were recognized throughout the whole LV, and in part in the right ventricular (RV) free wall. Although the entire thickness of LV wall was involve, the fibrosis was more marked in the subendocardial region compared with subepicardial region. Qualitatively similar results were obtained from the hearts with and without THIR. The fibrosis areas estimated from the azan-staining of 4 whole cross sections in each heart from the base to the apex (Fig. 1) were 12.7±4.4% and 12.2±4.8% in MI and MI+THIR groups, respectively ($n=5$, $P>0.05$). Thus, THIR did not affect the amounts of fibrosis.

3.2. Immunostained Cx43 GJs in LV myocardium

Confocal microscopy for Cx43 immunolabeling was carried out in 6 hearts from all the 4 animal groups. Fig. 2A shows the representative effects of THIR in the control heart (without MI creation). Longitudinal sections of LV free wall myocardium were labeled for Cx43 (stained green) and cadherin (stained red). In Control, Cx43 formed clusters of punctate immunofluorescence domains confined to well-organized intercalated disks running across the longitudinal axis (panel a, arrows). Cadherin labeling showed a similar distribution to Cx43 (panel b). Double staining revealed the co-existence of Cx43 GJs and cadherin-containing fascia adherents confined to the intercalated disks, giving rise to their yellowish staining (panel c). In a rabbit 2 weeks after radiation (C+THIR), in contrast, Cx43 labeling was distributed not only at the intercalated disk but also at the lateral aspect of myocytes (panel d, arrowheads), whereas the normal distribution of cadherin was preserved (panel e).

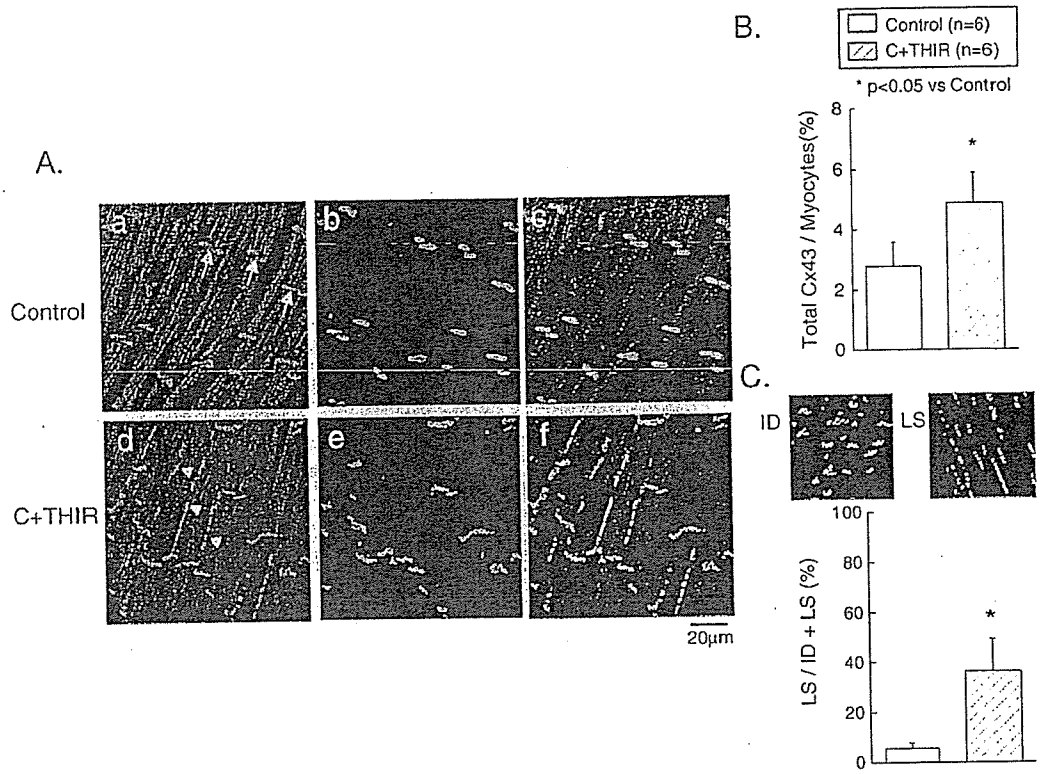

Fig. 2. Immunostained Cx43 gap junctions and fasciae adherentes in the LV myocardium of rabbits without MI. A, An LV myocardium sectioned longitudinally was labeled for Cx43 (green) and cadherin (red). Top, a section from a control heart; bottom, a section from a heart after targeted heavy ion irradiation (THIR). All images are single optical slices (confocal laser microscopy). Scale bar, 20 μm. B, The proportion of the total cell area occupied by Cx43 immunoreactive signal. Average values of 5 fields in each sample was obtained, and then means±SD of the values were calculated for each 6 samples. *$P<0.05$ vs. Control. C, Changes in the proportion of Cx43 labeled at the intercalated disk region (ID) and lateral cell surface (LS). (means±SD). Data were obtained from 12 rabbits (6 in each group). *$P<0.05$ vs. Control.

Double staining confirmed the dissociation of Cx43 from the intercalated disks (panel f). Similar derangements (lateralization) of Cx43 distribution were recognized in all C+THIR group. Fig. 2B shows the proportion of total cell area occupied by Cx43 immunoreactive signals. The radiation resulted in a significant increase in the Cx43 immunoreactive signals of 76%. Fig. 2C shows the proportion of Cx43 labeling at the lateral cell surface over the total labeling. The value in C+THIR was significantly higher (by 535%) than Control.

Fig. 3 show the effects of THIR on MI hearts. Representative changes of Cx43 immunolabeling patterns were compared in Fig. 3A at a low and a high magnification. In an MI heart (left), normal Cx43 labeling confined to the intercalated disks was preserved in the area distant from the infarcted tissue (patchy loss of myocytes indicated by arrowheads) (panels a, and c). In the area neighboring the infarcted tissue, Cx43 labeling was characterized either by prominent disorganization (panel e) or depletion (panel d). In an MI+THIR heart (right), immunoreactive Cx43 signals were increased throughout all of the LV tissues. This upregulation was recognized not only in the normal zone distant from the patchy infarcted tissue (panel f), but also in the periinfarct regions (panels g and h). The punctate Cx43 immunolabeling was distributed over the intercalated disk regions as well as lateral abutments of myocytes. Fig. 3B shows the proportion of total cell area occupied by the Cx43 immunoreactive signal obtained from the MI and MI+THIR groups. The irradiation resulted in a significant increase in Cx43 immunoreactive signals of 76%.

3.3. *Expression of Cx43 mRNA and protein in the LV myocardium*

The Cx43 mRNA level by a real-time PCR assay in the C+THIR specimens was significantly larger than that in Control specimens (by 18%) (Fig. 4A). The level in MIs, in contrast, decreased significantly compared with Controls (by 33%). Irradiation of MI rabbits (MI+THIR) reversed the downregulation of Cx43 mRNA and increased by 88% compared with MI.

Cx43 protein amounts were estimated by Western blotting (Fig. 4B). The Cx43 antibodies recognized two bands migrating between 42 and 47 kDa. The Cx43 immunoblot signals were quantified by densitometry, and the intensity was normalized to that of α-tubulin on the same membrane. Irradiation of control rabbits (C+THIR) caused a significant increase in the total amount Cx43 protein by 88% compared with Control animals. In MI rabbits, the total Cx43 protein

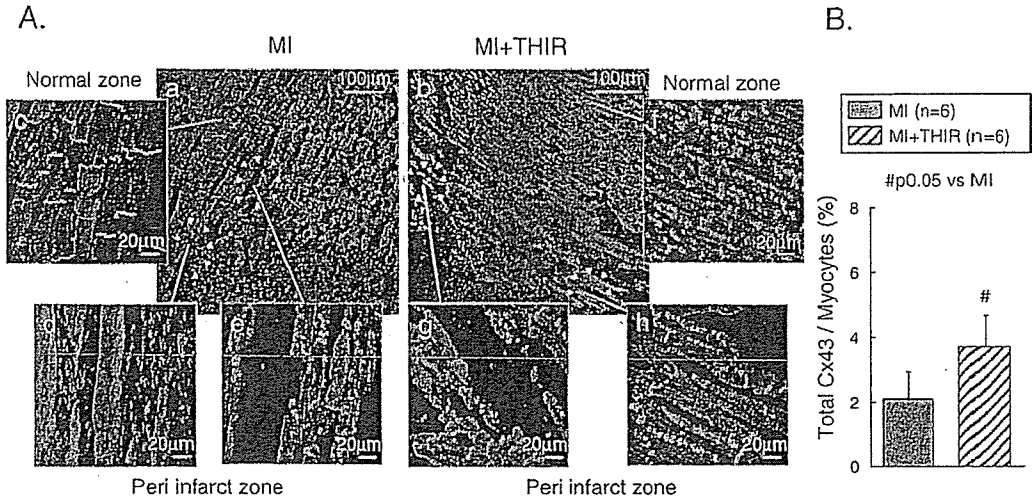

Fig. 3. Immunostained Cx43 gap junctions in the LV myocardium of rabbits with non-transmural MI. A, Left, a section from an MI heart; right, a section from a heart from MI+THIR. All images are single optical slices. Scale bar is 100 μm in panels (a) and (b), and 20 μm in panels (c) through (h). B, The proportion of total cell area occupied by Cx43 immunoreactive signal. Average values of 5 fields in each sample was obtained, and then means±SD of the values were calculated for each 6 samples. Data were obtained from 12 rabbits (6 in each group). #$P<0.05$ vs. MI.

levels significantly decreased compared with Controls (by 95%), and irradiation of MI rabbits (MI+THIR group) increased the level by 133% in comparison with unirradiated MI rabbits. We also estimated the density of the higher and lower molecular weight bands separately, which correspond to phosphorylated (P) and non-phosphorylated (NP) isoforms of Cx43, respectively. Irradiation caused appreciable increases in both Cx43-P and Cx43-NP in Control as well as in MI

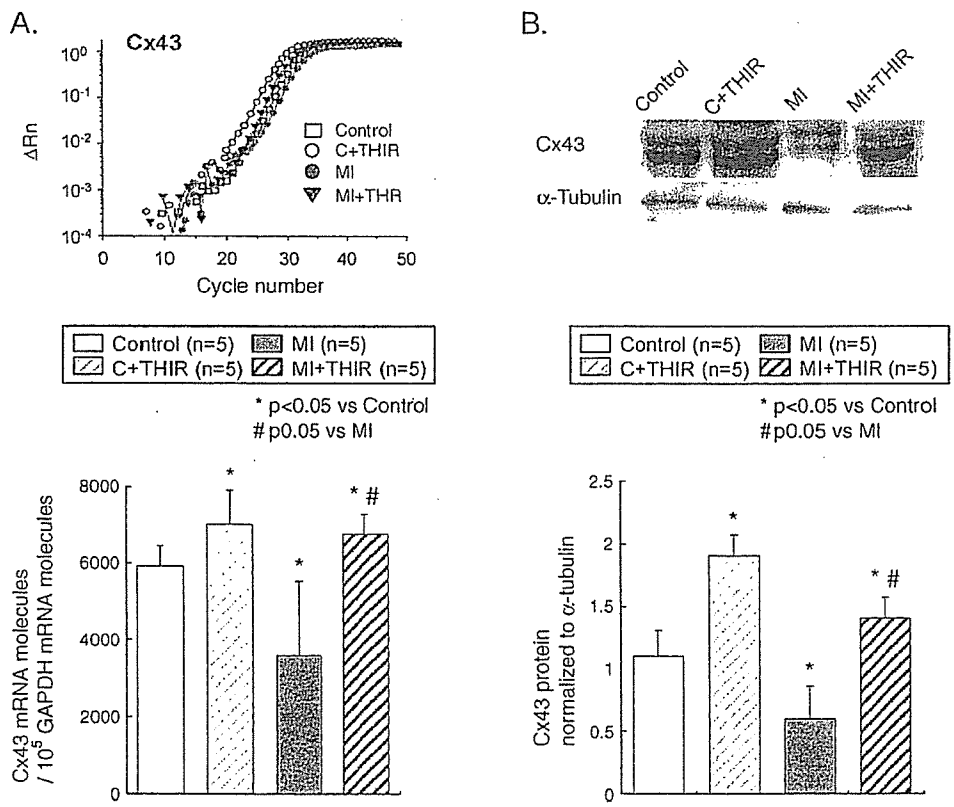

Fig. 4. Cx43 mRNA and protein levels. A, Cx43 mRNA levels were estimated by a real-time PCR and normalized to GAPDH. Top: Representative Cx43 PCR amplification plots for reactions. Change in fluorescence signal (ΔRn) is plotted against cycle number. Bottom: Cx43 mRNA levels normalized to GAPDH mRNA. Values are means±SD of each 5 rabbits in the 4 animal groups. B, Cx43 protein levels were estimated by Western blotting and normalized to α-tubulin. Values are means±SD of each 5 rabbits in the 4 animal groups. *$P<0.05$ vs. Control. #$P<0.05$ vs. MI.

rabbits. There were no significant differences among the four groups in the averaged ratio of P/NP (Control, 0.60; C+THIR, 0.84; MI, 1.00; MI+THIR, 0.96). Taken together, heavy-ion irradiation caused significant up-regulation of both mRNA and total protein levels of Cx43 in control as well as in MI hearts.

3.4. In-vivo electrophysiology

Fig. 5B illustrates representative AT and ARI maps on the LV anterior surface during the sinus rhythm (heart rate 197–238 bpm). In a Control rabbit, the activation proceeded quickly from paraseptal to lateral direction; TAT in the mapped area was 12 ms. ARIs were almost uniform, giving rise to a small ARID of 17 ms. In a C+THIR rabbit, the activation proceeded similarly (TAT 10 ms), but ARIs were homogeneously prolonged with ARID of 18 ms. In an MI rabbit, the activation proceeded much more slowly (TAT 32 ms). The ARI map showed tremendous regional variation, and ARID was increased up to 32 ms. In an MI+THIR rabbit, the AT map showed faster propagation (TAT 14 ms), and ARIs were more homogeneous than MI, causing less ARID (21 ms).

Data obtained from the 4 groups are summarized in Table 1. TAT was unchanged in C+THIR, but increased significantly in MI (by 89% from Control). The TAT in MI+THIR was significantly less than MI (by 42%), suggesting a reversal of the conduction delay. Both RI and ARI were significantly increased in C+THIR (by 10% and 11%, respectively). MI caused an appreciable prolongation of RT without affecting ARI compared with Control. In MI rabbits, RT and ARI were increased moderately after irradiation (MI+THIR), but the differences did not reach a statistical significance. In control rabbits, ARID was unaffected by irradiation. MI caused a significant increase in ARID (by 81%), and irradiation reversed the change.

Anisotropic conduction properties in the epicardial surface were examined in the 4 animal groups under constant pacing (cycle length of 200 ms) (Fig. 5C, D). In Control, the activation front proceeded at the highest speed in a direction parallel (longitudinal, L) to the subepicardial fiber orientation and at the slowest speed in a direction perpendicular to that (transverse, T). The isochrones showed an elliptical activation pattern. In the heart from a C+THIR rabbit, the elliptical

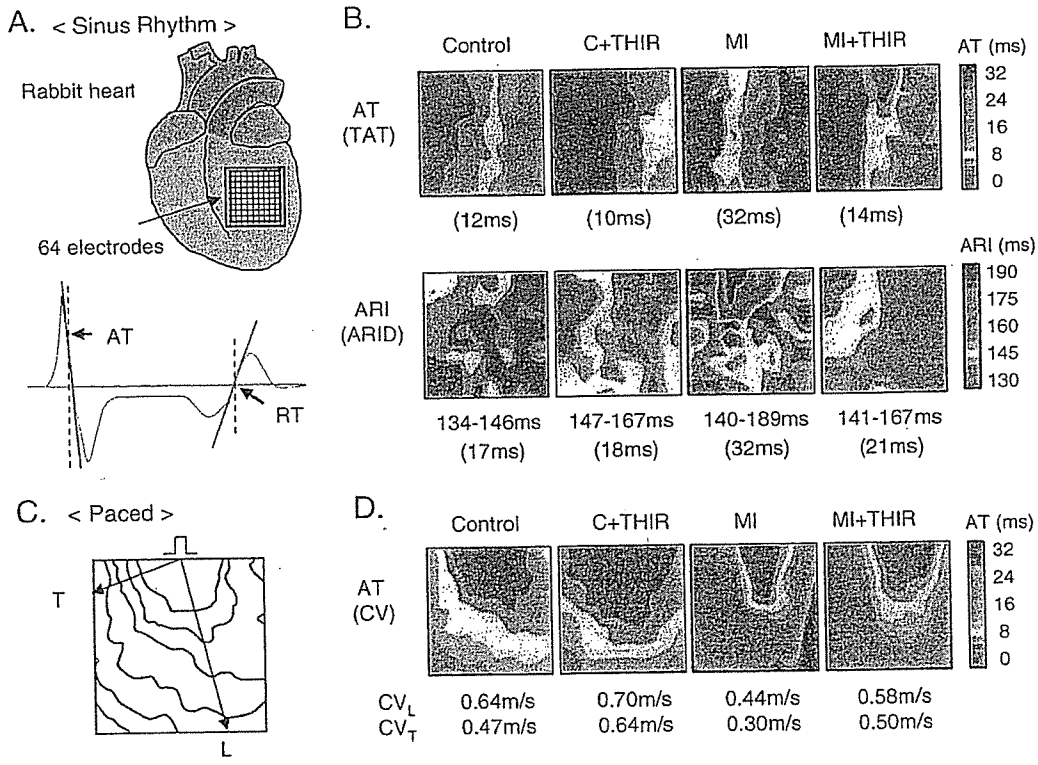

Fig. 5. Epicardial LV potential mapping. A, Sixty four monopolar electrodes were arranged as an 8×8 array to acquire the signals. Activation time (AT) at the recording site was identified by the initial sharp negative deflection (min dV/dt) of QRS. Recovery time (RT) was identified by the maximum upstroke slope (max dV/dt) of T wave. The time difference between AT and RT in each electrogram was measured for activation-recovery interval (ARI). B, Representative maps of AT and ARI during sinus rhythm. Total activation time (TAT) was measured from the maximal difference of AT. The dispersion of ARI (ARID) was estimated by the standard deviation of ARI at 64 electrodes. C, Anisotropic conduction properties were examined under constant pacing from the top middle of the electrode array. A line for longitudinal (L) propagation was drawn from the pacing site to the outer edge of the map, so as to cross the most widely spaced isochrones. A second line for transverse (T) propagation was drawn perpendicular to the first one. D, Representative maps of AT during the constant pacing. Conduction velocity in L and T direction (CV_L, CV_T) were measured from the isochrone maps.

Table 1
In-vivo electrophysiology

	Control (n=5)	C+THIR (n=5)	MI (n=5)	MI+THIR (n=5)
<*Sinus rhythm*>				
TAT (ms)	8.7±1.8	8.1±1.3	16.4±7.7*	9.5±2.7#
ARI (ms)	142±10	157±5*	146±18	160±8*
RT (ms)	150±10	165±6*	162±21*	169±8*
ARID (ms)	16.6±4.4	19.3±4.6	30.0±14.5*	18.8±4.5#
<*Paced*>				
CV_L (m/s)	0.66±0.14	0.72±0.18	0.48±0.10*	0.61±0.06#
CV_T (m/s)	0.45±0.04	0.67±0.20*	0.34±0.10*	0.51±0.09#
L/T	1.47±0.19	1.12±0.35*	1.54±0.61	1.22±0.19

Electrophysiological recordings were made in control rabbits without irradiation (Control, n=5), control rabbits after irradiation (C+THIR, n=5), myocardial infarction (MI) rabbits without irradiation (MI, n=5), and MI rabbits after irradiation (MI+THIR, n=5). Data were obtained either during sinus rhythm or under constant pacing at a cycle length of 200 ms. Values are means±SD. TAT, total activation time; RT, recovery time; ARI, activation-recovery interval; ARID, dispersion of ARI; CV_L, conduction velocity in longitudinal direction; CV_T, conduction velocity in transverse direction; L/T, anisotropic ratio of the conduction velocity. *P<0.05 vs. Control, #P<0.05 vs. MI.

pattern was less marked (more circular) because of acceleration of T propagation. In the heart from an MI rabbit, both L and T propagations were slowed down compared to Control, and the elliptical shape was slightly enhanced. In an MI+THIR rabbit, the activation pattern was more circular compared with MI alone, because of an acceleration of T propagation, which was more remarkable than the acceleration of L propagation. CVs in L and T directions (CV_L, CV_T) are summarized in Table 1. In control rabbits, irradiation caused a significant increase only in CV_T (by 49%), resulting in a significant decrease of the anisotropic ratio (L/T). In MI rabbits, both CV_L and CV_T were decreased compared with Control. Irradiation to MI rabbits (MI+THIR) caused significant increases of both CV_L and CV_T, but the change in CV_T (by 50%) was larger than that in CV_L (by 27%), resulting in a moderate reduction of L/T.

VT/VF induction was attempted by programmed stimulation in each 5 rabbits from the 4 animal groups. Representative ECG records in a Control, an MI and an MI+THIR rabbit are shown in Fig. 6A. Fig. 6B shows AT maps of 2 sequential beats during the VT/VF documented from the MI and MI+THIR rabbits. Fig. 6C summarizes the VT/VF incidence. In Control and C+THIR, no VT/VF was induced. In MI, 2 VF and 2 VT (one sustained >30 s, the other non-sustained) were induced. In MI+THIR, only one non-sustained VT (NSVT) was induced. Activation patterns during the NSVT were much more homogeneous than that during VF documented in MI rabbits (Fig. 6B).

3.5. Safety of irradiation

In both control and MI rabbits, THIR did not affect the hemodynamic parameters in echocardiography 2 weeks after the irradiation. The LV function in MI hearts was inhibited

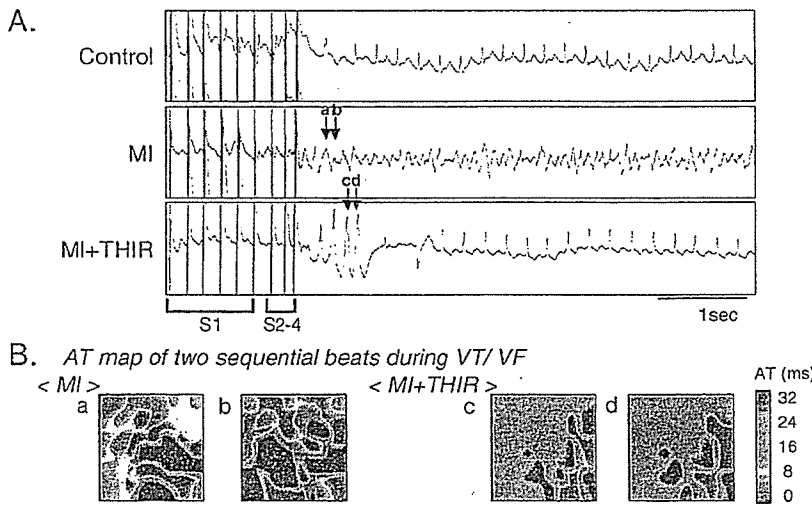

	NSVT	SVT	VF	Vulnerability
Control (n=5)	0	0	0	0/5
C+THIR (n =5)	0	0	0	0/5
MI (n= 5)	1	1	2	4/5
MI+THIR (n=5)	1	0	0	1/5

Fig. 6. Induction of VT/VF by programmed stimulation under norepinephrine infusion (0.1 μg/kg/min, i.v.). A, Representative ECG recordings in Control, MI and MI+THIR rabbits. Following 5 basic stimuli (S1) at a cycle length of 200 ms, triple extra stimuli (S2–S4) were applied at progressively shorter coupling intervals. B, AT maps of two sequential beats during the VF and VT episodes in the MI and MI+THIR rabbits as presented in A. C, Incidence of VT/VF elicited by the programmed stimulation. SVT: sustained VT (>30 s), NSVT: non-sustained VT (<30 s). VFs were all sustained.

significantly compared with Control, and the irradiation did not ameliorate the hemodynamic parameters (online data supplement). Blood cell counts and chemistry were unaffected by the irradiation. However a circumscribed loss of hair began to appear on the left anterior chest soon after irradiation and remained for a year.

4. Discussion

4.1. The novel findings

Immunoreactive Cx43 fluorescent signals of MI hearts were reduced and disorganized notably. In addition, the Cx43 mRNA level and the amount of Cx43 protein in LV tissue, which were estimated by a real-time PCR and Western blotting, respectively, were markedly reduced in MI hearts. Most of these changes were reversed 2 weeks after THIR. *In-vivo* 64Map revealed that a reduction of CV in MI hearts was reversed by THIR. An increase of ARID in MI hearts was reversed by THIR. An increase of vulnerability for VT/VF induction by programmed stimulation in MI hearts was also reversed by THIR. All of these observations can be interpreted most likely by an improvement of electrical coupling of cardiac myocytes, causing a smoother propagation of excitation and homogeneous repolarization in the ventricle after MI.

Achieving up-regulation of Cx43 in the myocardium might be a target for novel antiarrhythmic therapies. The use of radiation to up-regulate the decreased Cx43 in diseased hearts has never been considered. Radiotherapy might be one of the only potential approaches for future therapeutic strategy through achieving an increase in the electrical coupling of cardiac cells via the up-regulation of GJs.

4.2. Functional consequences of Cx43 up-regulation and lateralization

In normal as well as in MI hearts, THIR caused up-regulation of Cx43 and an increase of Cx43 distribution at the lateral cell abutments (lateralization). These changes would have a variety of functional consequences. The activation maps under constant pacing showed that the irradiation increased CVs and the effect was greater in T than L propagation, giving rise to a reduction of the anisotropic ratio (L/T). This observation suggests that Cx43 up-regulated and distributed more laterally may form functional GJs even though Cx43 was dissociated from cadherin. In rat atria in which atrial fibrillation (AF) was induced by 24 h of rapid pacing, Polontchouk et al. [13] showed up-regulation and marked lateralization of immunoreactive Cx43, like in human AF patients. The Cx43 remodeling was associated with a greater increase of CV_T than CV_L, resulting in a reduction of the anisotropic ratio. In experiments using isolated normal ventricular myocardium, pharmacological uncoupling of GJs (by heptanol or palmitoleic acid) was shown to cause greater inhibition of T propagation than L propagation [14,15]. A higher susceptibility of T propagation than L propagation in response to GJ uncoupling was also demonstrated in a computer simulation [16]. Accordingly, the total up-regulation of Cx43 by THIR could also contribute to the preferential improvement of T propagation.

It appears that lateralization of gap junctions is a prominent feature of diseased hearts, including a variety of ischemic and hypertrophic cardiomyopathies [1,16]. Functional implication of this feature is variable. In experiments using aged rabbits, Dhein and Hammerrath [17] found reduced CV_T and enhanced anisotropy (CV_L was preserved). Those changes were associated with prominent increase of fibrosis separating myocardial cells and lateralization of Cx43. The extensive fibrosis might have offset the effects of GJ lateralization. Alternatively, the displaced Cx43 GJs could be degraded and non-functional [1]. Since we used young rabbits in the present study, the control hearts with and without THIR had no appreciable collagen strands separating myocardial fibers. In MI hearts, in contrast, there existed substantial amounts of fibrosis at the regions of patchy infarction. Despite of such fibrosis, THIR improved the T propagation.

As to the role enhanced GJ lateralization in arrhythmogenesis, there are 2 possibilities. If the GJs function normally, they would ameliorate the inhibition of T propagation resulting from functional and structural uncoupling of cardiac cells, and may reduce the risk for microscopic anisotropic reentry based on the extremely slow T propagation [18,19] and the lateral inhomogeneity of repolarization. The present results seem consistent with this prediction. If the lateral GJs are degraded and non-functional, the conductivity and electrical homogeneity of the heart will be hampered by the dislocation in favor of reentrant excitations. In a simulation study using a two-dimensional model of myocardial cell architecture, Spach and Heidlage [20] suggested the stochastic nature of normal propagation at a microscopic level based on the normal polar distribution of GJs provides a considerable protective effect against arrhythmias by reestablishing the general trend of wave-front movement after small variations in excitation events occur.

Cx43 is a phosphoprotein, and phophorylation/dephosphorylation of Cx43 plays important roles in the regulation of Cx43 protein turnover dynamics (trafficking, plaque assembly, disassembly and degradation) as well as GJ channel gating properties [21]. We estimated the relative expression of P and NP isoforms of Cx43 from 2 bands recognized in Western blotting. The results may suggest that THIR increases both Cx43-P and Cx43-NP without affecting their P/NP ratio. However, more extensive Western blots using isoform-specific Cx43 antibodies will be required to resolve the issue.

4.3. Mechanisms of Cx43 up-regulation by irradiation

In the field of oncology, it has been demonstrated in many *in-vitro* and *in-vivo* studies that intercellular communication

is enhanced by photon [2,3] or ionizing radiation [22,23] via up-regulation of Cx43 GJs at mRNA and protein levels. The increase of intercellular communication is believed to play an important role for the enhancement of radiation-induced effects such as modulation of gene expression, mutagenesis and cell survival (bystander effect) [24–26]. As to the molecular mechanisms responsible for the radiation-induced Cx43 up-regulation, the information available is still limited. Using deletion and site-directed mutagenesis analyses in human fibroblasts and HeLa cells, Glover et al. have demonstrated that 2 consensus sites, nuclear factor of activated T-cells (NFAT) and activator protein (AP1), are responsible for the major activation of the Cx43 promoter in response to low doses of ionizing radiation [23] A similar molecular mechanism could be involved in the THIR-induced up-regulation in mammalian cardiac cells, but the issue remains to be investigated.

4.4. What other methods could be considered to achieve similar results?

Several procedures have been proposed by previous investigators to increase the electrical coupling of ventricular myocytes through an increase of Cx43 protein. Those include endothelin-1, angiotensin-II, thyroid hormones, AAP10 and nitrofen [27–30]. As to the therapeutic challenge to ameliorate arrhythmogenic substrates, however, all of these procedures have significant limitations in their clinical feasibility because of their low efficiency, undesirable cardiovascular and other side effects. We believe that THIR might be the first clinically feasible procedure, although further experimental studies using large animals will be required to substantiate this proposal.

4.5. Limitations

1) Because the rabbit heart is smaller and the heart rate is faster than human, higher irradiation accuracy was demanded in the present study. It was practically difficult to synchronize the heart motion completely to correspond to the radiation release. In addition to the targeted anterolateral LV free wall, other regions of LV might have been subjected to the irradiation. 2) The time dependent expression of Cx43 and the minimum irradiation energy for the appearance of the first antiarrhythmic effect were not examined.

5. Conclusion

Heavy-ion energy increases Cx43 expression of the ventricle in MI rabbits and consequently improves the conductivity, decreases the spatial heterogeneity of repolarization, and reduces the VT/VF vulnerability. Targeted heavy-ion irradiation to the heart could have the potential to become a new antiarrhythmic preventive therapy for MI patients through the restoration of cell-to-cell electrical coupling.

Acknowledgments

This work was supported by Grants-in-Aid for Scientific Research (B) 17390236 from JSPS and Tokai University School of Medicine Research Aid. We are grateful to many colleagues for their technical support: Atsushi Matsuzaki, Kazutane Usui, Yoshiaki Deguchi, Yuji Ikari, Nobue Kumaki, Sachie Tanaka, Noboru Kawabe, Hideaki Hasegawa, Yoshiro Shinozaki, Jobu Itoho in Tokai University; Jong-Kook Lee, Yoshiko Takagishi, Akiko Matsumiya, Kyoko Harada, Mayumi Hojo in Nagoya University; Takeshi Murakami, Kumie Nojima in the HIMAC Cooperative Research Project; Norio Sugimoto in the SANWAKAGAKU laboratory; Norihiko Mishima, Masaya Sakai, Satoshi Yamazaki in FUKUDA DENSHI,. Co Ltd; Daisuke Araki, Takashi Akamatsu, Michinari Kaneko in UNIQUE MEDICAL,. Co Ltd; and Daisuke Nakata in Ela Medical,. Co Ltd.

Appendix A. Supplementary data

Supplementary data associated with this article can be found, in the online version, at doi:10.1016/j.cardiores.2006.09.010.

References

[1] Severs NJ, Coppen SR, Dupont E, Yeh HI, Ko YS, Matsushita T. Gap junction alterations in human cardiac disease. Cardiovasc Res 2004;62:368–77.
[2] Liu K, Kasper M, Bierhause A, Langer S, Muller M, Trott KR. Connexin 43 expression in normal and irradiated mouse skin. Radiat Res 1997;147:437–41.
[3] Kasper M, Traub O, Reimann T, Bjerner L, Grossmann H, Muller M, et al. Upregulation of gap junction protein connexin 43 in alveolar epithelial cells of rats with radiation-induced pulmonary fibrosis. Histochem Cell Biol 1996;106:419–24.
[4] Kanai T, Endo M, Minohara S, Miyahara N, Koyama I, Tomura H, et al. Biophysical characteristics of HIMAC clinical irradiation system for heavy-ion radiation therapy. Int J Radiat Oncol Biol Phys 1999;44:201–10.
[5] Debus J, Jackel O, Kraft G, Wannenmacher M. Is there a role for heavy ion beam therapy? Recent Results Cancer Res 1998;150:170–82.
[6] Koike S, Ando K, Oohira C, Fukawa T, Lee R, Takai N, et al. Relative biological effectiveness of 290 MeV/u carbon ions for the growth delay of a radioresistant murine fibrosarcoma. J Radiat Res 2002;43:247–55.
[7] Tanaka E, Hattan N, Ando K, Ueno H, Sugio Y, Mohammed MU, et al. Amelioration of microvascular myocardial ischemia by gene transfer of vascular endothelial growth factor in rabbits. J Thorac Cardiovasc Surg 2000;120:720–8.
[8] Niwa N, Yasui K, Opthof T, Takemura H, Shimuzu A, Horiba M, et al. $Ca_v3.2$ subunit underlies the functional T-tye Ca^{2+} channel in murine hearts during the embryonic period. Am J Physiol 2004;286:H2257–63.
[9] Uzzaman M, Honjo H, Takagishi Y, Emdad L, Magee AI, Severs NJ, et al. Remodeling of gap junctional coupling in hypertrophied right ventricles of rats with monocrotaline-induced pulmonary hypertension. Circ Res 2000;86:871–8.
[10] Yoshioka K, Amino M, Usui K, Sugimoto A, Matsuzaki A, Kohzuma K, et al. Nifekalant hydrochloride administration during cardiopulmonary resuscitation improves the transmural dispersion of myocardial repolarization. Circulation J 2006;70:1200–7.
[11] Yoshioka K, Gao DW, Chin M, Stillson C, Penades E, Lesh M, et al. Heterogeneous sympathetic innervation influences local myocardial repolarization in normally perfused rabbit hearts. Circulation 2000;101:1060–6.

[12] Dhein S, Muller A, Gerwin R, Klaus W. Comparative study on the proarrhythmic effects of some antiarrhythmic agents. Circulation 1993;87:617–30.
[13] Polontchouk L, Haefliger J-A, Ebelt B, Schaefer T, Stuhlmann D, Mehlhorn U, et al. Effects of chronic atrial fibrillation on gap junction distribution in human and rat atria. J Am Coll Cardiol 2001;38:883–91.
[14] Delmar M, Michaels DC, Johnson T, Jalife J. Effects of increasing intercellular resistance on transverse and longitudinal propagation in sheep epicardial muscle. Circ Res 1987;60:780–5.
[15] Dhein S, Krusemann K, Schaefer T. Effects of the gap junction uncoupler palmitoleic acid on the activation and repolarization wavefronts in isolated rabbit hearts. Br J Pharmacol 1999;128:1375–84.
[16] Jongsma HJ, Wilders R. Gap junctions in cardiovascular disease. Circ Res 2000;86:1193–7.
[17] Dhein S, Hammerath S-B. Aspects of the intercellular communication in aged hearts: effects of the gap junction uncoupler palmitoleic acid. Naunyn-Schmiedeberg's Arch Pharmacol 2001;364:397–408.
[18] Spach MS, Josephson ME. Initiating reentry: the role of nonuniform anisotropy in small circuits. J Cardiovasc Electrophysiol 1994;5:182–209.
[19] Koura T, Hara M, Takeuchi S, Ota K, Okada Y, Miyoshi S, et al. Anisotropic conduction properties in canine atria analyzed by high-resolution optical mapping. Preferential direction of conduction block changes from longitudinal to transverse with increasing age. Circulation 2002;105:2092–8.
[20] Spach MS, Heidlage JF. The stochastic nature of cardiac propagation at a microscopic level. Electrical description of myocardial architecture and its application to conduction. Circ Res 1995;76:366–80.
[21] Lampe PD, Lau AF. The effects of connexin phosphorylation on gap junctional communication. Int J Biochem Cell Biol 2004;36:1171–86.
[22] Azzam EI, de Toledo SM, Gooding T, Little JB. Intercellular communication is involved in the bystander regulation of gene expression in human cells exposed to very low fluences of alpha particles. Radiat Res 1998;150:497–504.
[23] Glover D, Little JB, Lavin MF, Gueven N. Low dose ionizing radiation-induced activation of connexin43 expression. Int J Radiat Biol 2003;79:955–64.
[24] Azzam EI, de Toledo SM, Little JB. Expression of connexin 43 is highly sensitive to ionizing radiation and other environmental stresses. Cancer Res 2003;63:7128–35.
[25] Little JB, Azzam EI, de Toledo SM, Nagasawa H. Bystander effects: intercellular transmission of radiation damage signals. Radiat Prot Dosim 2002;99:159–62.
[26] Azzam EI, de Toledo SM, Little JB. Direct evidence for the participation of gap junction-mediated intercellular communication in the transmission of damage signals from alpha-particle irradiated to nonirradiated cells. PNAS 2001;98:473–8.
[27] Polontchouk L, Ebelt B, Jackels M, Dhein S. Chronic effects of endothelin 1 and angiotensin II on gap junctions and intercellular communication in cardiac cells. FASEB J 2002;16:87–9.
[28] Tribulova N, Shneyvays V, Mamedova LK, Moshel S, Zinman T, Shainberg A, et al. Enhanced connexin-43 and alpha-sarcomeric actin expression in cultured heart myocytes exposed to triiodo-L-thyronine. J Mol Histol 2004;35:463–70.
[29] Muller A, Schaefer T, Linke W, Tudyka T, Gottwald M, Klaus W, et al. Actions of the antiarrhythmic peptide AAP10 on intercellular coupling. Naunyn-Schmiedeberg's Arch Pharmacol 1997;356:76–82.
[30] Gonzalez-Reyes S, Fernandez-Dumont V, Calonge WM, Martinez L, Tovar JA. Expression of Connexin 43 in the hearts of rat embryos exposed to nitrofen and effects of vitamin A on it. Pediatr Surg Int 2006;22:61–5.

The EMBO Journal (2006) 25, 2315–2325 | © 2006 European Molecular Biology Organization | All Rights Reserved 0261-4189/06
www.embojournal.org

THE EMBO JOURNAL

Crystal structure of CHP2 complexed with NHE1-cytosolic region and an implication for pH regulation

Youssef Ben Ammar[1,4], Soichi Takeda[2,3,4], Takashi Hisamitsu[1], Hidezo Mori[2] and Shigeo Wakabayashi[1,*]

[1]Department of Molecular Physiology, National Cardiovascular Center Research Institute, Suita, Osaka, Japan, [2]Department of Cardiac Physiology, National Cardiovascular Center Research Institute, Suita, Osaka, Japan and [3]Laboratory of Structural Biochemistry, RIKEN Harima Institute at SPring-8, Kouto, Mikazuki-cho, Sayo, Hyogo, Japan

The plasma membrane Na^+/H^+ exchangers (NHE) require calcineurin B homologous protein (CHP) as an obligatory binding partner for ion transport. Here, we report the first crystal structure of CHP (CHP2 isoform) in complex with its binding domain in NHE1. We show that the cytoplasmic α-helix of NHE1 is inserted into the hydrophobic cleft formed by N- and C-lobes of CHP2 and that the size and shape of this crevice together with hydrogen bond formation at multiple positions assure a high degree of specificity for interaction with NHE members. Structure-based mutagenesis revealed the importance of hydrophobic interactions between CHP/NHE1 for the function of NHE1. Furthermore, the crystal structure shows the existence of a protruding CHP-unique region, and deletion of this region in CHP2 inhibited the NHE1 activity by inducing the acidic shift of intracellular pH dependence, while preserving interaction with NHE1. These findings suggest that CHP serves as an obligatory subunit that is required both for supporting the basic activity and regulating the pH-sensing of NHE1 via interactions between distinct parts of these proteins.

The EMBO Journal (2006) 25, 2315–2325. doi:10.1038/sj.emboj.7601145; Published online 18 May 2006

Subject Categories: membranes & transport; structural biology

Keywords: calcineurin homologous protein; crystal structure; Na^+/H^+ exchanger; pH regulation

Introduction

Maintenance of intracellular pH (pH_i), Na^+ concentration, and cell volume is crucial for all living cells to survive and to ensure a variety of cellular functions, such as cell metabolic processes, muscle contraction, secretion, and higher-order brain activity. The Na^+/H^+ exchanger (NHE) is an important transporter regulating such ionic homeostasis and catalyzing the electroneutral countertransport of Na^+ and H^+ through the plasma membrane and other intracellular organellar membranes in various animal species (Wakabayashi *et al*, 1997; Counillon and Pouyssegur, 2000; Putney *et al*, 2002; Orlowski and Grinstein, 2004; Zachos *et al*, 2005). Of the nine different NHE isoforms identified to date (NHE1–NHE9), the ubiquitous isoform NHE1 has been studied most extensively. NHE1 is known to be activated rapidly in response to various extracellular stimuli, such as hormones, growth factors, and mechanical stressors (Wakabayashi *et al*, 1997; Orlowski and Grinstein, 2004). Such activation of NHE1 is often linked to various diseases. For example, elevated NHE1 activity is thought to be a risk factor causing heart failure and hypertrophy, as evidenced by the remarkable protective effects of specific inhibitors (Karmazyn, 2001; Engelhardt *et al*, 2002). Regulation of NHE1 is thought to occur through interaction of multiple signaling molecules with the carboxyl (C)-terminal cytoplasmic domain of NHE1 and subsequent conformational change of the amino (N)-terminal transmembrane domain responsible for catalyzing NHE (see Figure 1A for membrane topology). Importantly, this regulation of NHE1 is attributable to a change in the affinity for intracellular H^+. A previous biochemical experiment using membrane vesicles suggested that the exchangers possess a cytoplasmic 'H^+-modifier' or 'pH-sensor' site(s), distinct from the H^+-transport site (Aronson *et al*, 1982; Wakabayashi *et al*, 2003a). The exchangers were thus considered to be activated through conformational changes caused by protonation of this regulatory site. Our recent study, using cells expressing NHE isoforms (NHE1–3), further supported this concept by measuring the reverse reaction of exchange (Na^+ efflux) (Wakabayashi *et al*, 2003a). However, another recent study reported an allosteric model with no additional H^+-modifier site to explain the sigmoidal cytosolic H^+ dependence (Lacroix *et al*, 2004).

Of the signaling molecules that interact with the exchanger, calcineurin B (CNB) homologous protein (CHP) is particularly important. CHP was initially identified as a protein (p22) involved in vesicular transport (Barroso *et al*, 1996) and that interacts with NHE (Lin and Barber, 1996). CHP is a Ca^{2+}-binding protein with EF-hand motifs and is myristoylated at the N-terminus (Gly2) (Barroso *et al*, 1996; Lin and Barber, 1996). To date, three CHP isoforms with different tissue expression patterns have been identified in mammalian tissues. While CHP1 is expressed ubiquitously in virtually all tissues, the expression of CHP2 is restricted to cancer cells (Pang *et al*, 2002) and the small intestine (Inoue *et al*, 2003), and that of CHP3 (also called tescalcin) is restricted to the heart, brain, stomach, and testis (Mailander *et al*, 2001; Perera *et al*, 2001; Gutierrez-Ford *et al*, 2003). Previously, we reported that CHP (at least CHP1 and CHP2) is an essential cofactor supporting the physiological activity of the plasmalemmal NHE by interacting with the juxtamembrane cyto-

*Corresponding author. Department of Molecular Physiology, National Cardiovascular Center Research Institute, Fujishirodai 5-7-1, Suita, Osaka 565-8565, Japan. Tel.: +81 6 6833 5012; Fax: +81 6 6835 5314; E-mail: wak@ri.ncvc.go.jp
[4]These authors contributed equally to this work

Received: 5 December 2005; accepted: 24 April 2006; published online: 18 May 2006

©2006 European Molecular Biology Organization

Table I Data collection, phasing and refinement statistics

	High resolution data	MAD		
Data collection				
Space group	$P4_3$	$P4_3$		
Cell dimensions				
a, *b*, *c* (Å)	49.96, 49.96, 103.2	49.96, 49.96, 103.2		
α, β, γ (deg)	90, 90, 90	90, 90, 90		
		Peak	*Inflection*	*Remote*
Wavelength	1.0000	0.7270	0.7266	1.0000
Resolution (Å)	50–2.7	50–3.0 (3.11–3.00)	50–3.0 (3.11–3.00)	50–3.0 (3.11–3.00)
R_{merge}[a]	4.8 (25.1)	0.084 (0.311)	0.073 (0.297)	0.072 (0.330)
$I/\sigma I$[b]	17.3 (4.5)	14.9 (4.1)	15.9 (5.0)	15.8 (3.6)
Completeness (%)[b]	97.3 (83.1)	98.5 (87.5)	98.5(87.5)	97.8 (80.9)
Redundancy[b]	4.0 (3.1)	7.2 (5.6)	7.3 (5.7)	7.1 (5.3)
Refinement				
Resolution (Å)	50–2.7			
No. reflections	6746			
R_{work}/R_{free}	0.218/0.287			
No. atoms				
Protein	1674			
Ligand/ion	2			
B-factors				
Protein	72.5			
Ligand/ion	70.5			
R.m.s. deviations				
Bond lengths (Å)	0.005			
Bond angles (deg)	1.00			
Ramachandran plot (%)				
Favorable	87.2			
Allowed	12.8			
Generously allowed	0			
Disallowed	0			

[a]$R_{merge} = \sum_{hkl} \sum_i |I_i(hkl) - \langle I(hkl) \rangle| / \sum_{hkl} \sum_i I_i(hkl)$, where $I_i(hkl)$ is the *i*th intensity measurement of reflection *hkl*, and $\langle I(hkl) \rangle$ is its average.
[b]Highest resolution shell is shown in parentheses.

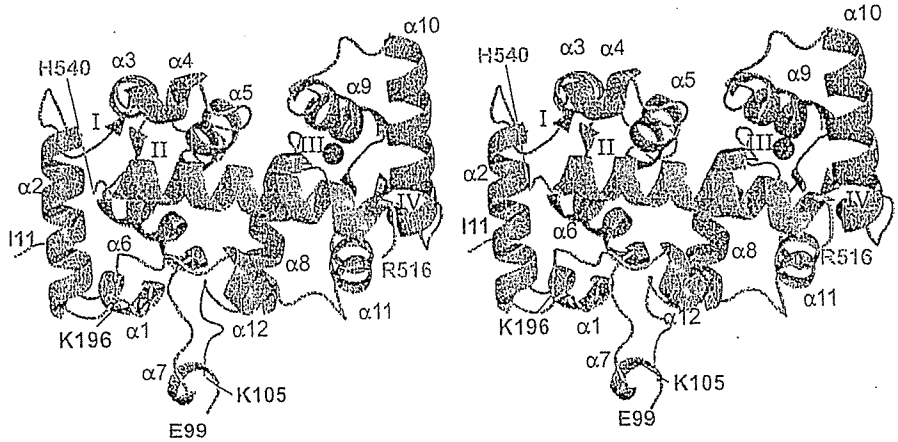

Figure 2 Stereo view of the CHP2/NHE1-peptide complex showing the overall structure. N- and C-lobes of CHP2 are colored *red* and *blue*, respectively. The NHE1 peptide is colored *green*. *Pink* spheres represent the two yttrium ions coordinated by EF3 and EF4.

the overall structure of the complex CHP2/NHE1-peptide. The structural model contains 181 amino acids from CHP2 (Ile11–Glu99 and Lys105–Lys196), and 25 amino acids from NHE1 fragment (Arg516–His540). The polypeptide chain of CHP2 with dimensions of 55 × 47 × 28 Å is folded into two globular domains (N- and C-terminal lobes) composed of 12 α-helices (α1–α12) and four short β-strands (β1–β4). Two Y^{3+} ions were found to associate with EF3 and EF4 in the C-lobe (Figure 2), consistent with biochemical data showing the high-affinity binding of Y^{3+} (~1 nM) to CHP2 (Supplementary Figure 1). The overall structure of CHP2 is close to the Ca^{2+}-bound form of NHE-free CHP1, which was solved recently (Naoe *et al*, 2005; Supplementary Figure 2). Indeed, the distances between metal ions and coordinating oxygen atoms are almost the same for Y^{3+} in CHP2 (2.38 ± 0.2 Å) and Ca^{2+} in CHP1 (2.40 ± 0.1 Å). In addition, the

©2006 European Molecular Biology Organization